



## Prediction and Experimental Validation of In-Plane Current Distribution Between Channel and Land in a PEFC

Jun Li,<sup>a</sup> Chao-Yang Wang,<sup>a,\*</sup> and Ay Su<sup>b</sup>

<sup>a</sup>Electrochemical Engine Center, and Department of Mechanical and Nuclear Engineering, The Pennsylvania State University, University Park, Pennsylvania 16802, USA

<sup>b</sup>Fuel Cell Center, Yuan-Ze University, Zhongli City, Taoyuan County 320, Taiwan

A nonisothermal, two-phase model for polymer electrolyte fuel cells is validated against the experimental data of in-plane current density profiles. Overall, good agreement is achieved between predicted and measured current density distributions between the channel and land with submillimeter resolution. Numerical simulations clearly show that the in-plane current profile results from the interplay between the ohmic control and mass transport control, both of which depend strongly on the two-phase water transport along the in-plane direction. Under relatively dry and large stoichiometric conditions, the current density peak is seen to shift from under the land to under the channel with increasing average current density, signifying control by membrane resistance at low current densities but by oxygen diffusion at high current densities. Finally, the validated model reveals the dramatic influence of the channel/land width and gas diffusion layer compression on the in-plane current density profile, thus underscoring the necessity to match these two key parameters in experimental measurements of in-plane current distribution.

© 2007 The Electrochemical Society. [DOI: 10.1149/1.2801977] All rights reserved.

Manuscript submitted June 29, 2007; revised manuscript received September 28, 2007.

Available electronically November 9, 2007.

Computational modeling of polymer electrolyte fuel cells (PEFCs) continues to advance rapidly. Following the comprehensive review of Wang,<sup>1</sup> there is a concerted effort worldwide to validate sophisticated multiphysics, multidimensional fuel cell models against distribution data, such as current and species distributions,<sup>2-4</sup> as well as simultaneous measurements of multiple parameters, including liquid water distributions.<sup>5,6</sup> However, all model validation to date was performed at the cell scale. Experimental validation of PEFC models at submillimeter scale has not been reported in the open literature due to a lack of such experimental data. Most recently, Freunberger et al.<sup>7</sup> presented a set of in-plane current distribution data over the channel and land in a differential cell measured by embedding Pt wires 0.5 mm apart between the gas diffusion layer (GDL) and catalyst layer (CL). In the present paper, we report a study to validate the  $M^2$  model widely disseminated in the literature<sup>8-10</sup> against this emerged data at submillimeter resolution. This validation exercise is also expected to shed light on the possible sources of errors and essential design requirements of micron-resolution current sensing techniques.

Understandably, prediction and control of the current distribution are critical to improve the power density of next-generation PEFCs. Nonuniform current distribution caused by inhomogeneous proton and reactant transport exists in all three dimensions: along the flow channels, in the in-plane direction between the channel and land, and across the CL thickness. Significant efforts have been expended to measure and predict the current distribution along the channel. For instance, Yang et al.<sup>11</sup> and Liu et al.<sup>12</sup> used a segmented cell to simultaneously measure the distributions of current density, species concentration and water transport coefficient through the membrane. Measuring and predicting the current distribution in the in-plane direction is vitally important as it provides the critical information of current partitioning between the channel and land areas and hence helps establish a rational guideline for the flow field design in terms of optimal channel and land widths. This is the subject of the present study. Along with the in-plane current density data of Freunberger et al.,<sup>7</sup> we employ a nonisothermal, two-phase model to explore the physics governing the in-plane current distribution between the channel and land, as well as to reveal the essential design requirements and potential sources of errors in submillimeter current distribution measurements.

### Model and Validation Experiment

**Numerical model.**—Based on the  $M^2$  framework, a two phase, nonisothermal PEFC model has been developed in the prior literature.<sup>8-10</sup> A salient feature of this model is able to capture the dry-to-wet transition in three dimensions without tracking multiple interfaces between single- and two-phase regions.<sup>10</sup> Basic assumptions of the present model include (i) ideal gas mixture; (ii) laminar and mist flow in gas channels, where water droplets are sufficiently small that they travel at the same speed as the gas; and (iii) isotropic and homogeneous membrane, CL and GDL. The model is briefly summarized in Table I, with other details, the model's constitutive relations, and boundary conditions referenced to Wang and Wang.<sup>9</sup>

**Experiments.**—The experimental technique and conditions used by Freunberger et al.<sup>7</sup> are briefly summarized here for completeness. The basic principle of their experimental method was to measure the electrical potential distribution along the CL/GDL interface and solve the electron transport equation in the cathode GDL as described by Laplace equation, thus yielding the current density profile between channel and land. The most important boundary condition, the potential profile at the cathode GDL/CL interface, was measured with gold wires 25  $\mu\text{m}$  in diameter and 0.5 mm apart by assuming that the local fuel cell conditions and electrical potential were not disrupted by these wires. Both through- and in-plane electronic conductivity of GDL and the contact resistance between GDL and land were carefully calibrated in separate experiments and incorporated in the determination of in-plane current distribution. This study provided the data of potential and current density distributions in the submillimeter scale.

**Cell configurations.**—We consider two cells whose cross sections are shown in Fig. 1 along with the respective two-dimensional computational meshes. Cell A is identical to the experimental cell of 1  $\text{cm}^2$  active area used in Freunberger et al.<sup>7</sup> with two channels of 2 mm width, one inner rib and two outer ribs of 2 mm width. Both channel and rib widths are made larger than common PEFC designs to facilitate Pt wire embedment and experimental instrumentation. Hence, computationally we also consider cell B featuring a standard PEFC design with channel and rib widths both equal to 1 mm. To keep the same active area as cell A, cell B has four channels in the center, two half channels on the edge as well as five ribs, as shown in Fig. 1. Both cells are operated under sufficiently large stoichiometric ratios, thus rendering them differential cells where only the cross-sectional geometry is of interest. For both cells, the region enclosed by the dashed lines shown in Fig. 1a and b are the unit domain for computations. The total mesh consists of  $\sim 5000$  and

\* Electrochemical Society Active Member.

<sup>z</sup> E-mail: cwx31@psu.edu

**Table I. Two-phase, nonisothermal PEFC model: governing equations and source terms.**

	Conservation equations	Source terms
Mass	$\nabla \cdot (\rho \mathbf{u}) = 0$	
Momentum	$\frac{1}{\varepsilon^2} \nabla \cdot (\rho \mathbf{u} \mathbf{u}) = -\nabla p + \nabla \cdot \boldsymbol{\tau} + S_u$	In GDL and CL: $S_u = -(\mu/K)\mathbf{u}$
Energy	$\nabla \cdot (\gamma_T \rho C_p \mathbf{u} T) = \nabla \cdot (k^{\text{eff}} \nabla T) + S_T$	In CL: $S_T = j \left( \eta + T \frac{dU_0}{dT} \right) + \frac{i_c^2}{\kappa^{\text{eff}}} + \frac{i_s^2}{\sigma^{\text{eff}}} + h_{\text{fg}} \dot{m}_{\text{fg}}$ In GDL: $S_T = i_s^2 / \sigma^{\text{eff}} + h_{\text{fg}} \dot{m}_{\text{fg}}$ In membrane: $S_T = i_c^2 / \kappa^{\text{eff}}$ In bipolar plate: $S_T = i_s^2 / \sigma^{\text{eff}}$
Species	$\nabla \cdot (\gamma_c \mathbf{u} C^k) = \nabla \cdot (D_g^{\text{k,eff}} \nabla C_g^k) - \nabla \cdot \left[ \left( \frac{m_1^k}{M^k} - \frac{C_g^k}{\rho_g} \right) \mathbf{j}_1 \right] + S_k$	In CL: $S_k = -\nabla \cdot \left( \frac{n_d}{F} j_c \right) - \frac{S_k j}{n_k F}$
Proton	$\nabla \cdot (\kappa^{\text{eff}} \nabla \Phi_e) + j = 0$	
Electron	$\nabla \cdot (\sigma^{\text{eff}} \nabla \Phi_s) - j = 0$	

2000 for cells A and B, respectively. The dashed lines shown in Fig. 1c and d mark the channel regions. The governing equations listed in Table I are solved using commercial software FLUENT (version 6.1.22) in conjunction with the user defined functions developed for M<sup>2</sup> model at ECEC.

Computational cases considered in this study are listed in Table II. Cases 1 and 2 are designed for experimental validation where 30% relative humidity (RH) gases are fed to cell A with the oxidant being air and pure O<sub>2</sub>, respectively. Cases 3 and 4 are intended to study the in-plane current distribution in the standard PEFC (cell B) under similar operating conditions. In addition, case 5 permits discernment of differences between dry (30% RH) and fully humidified (100% RH) conditions. All the geometrical and operational parameters are listed in Table III. The stoichiometric ratios on both anode and cathode are sufficiently high that there is no variation along the channel, resulting in a differential cell configuration. This also justifies the validity of the assumption that water droplets are tiny and mist flow occurs in gas channels.

In all results shown below, the in-plane current density profile is calculated in the middle of the membrane using the electrolyte phase potential gradient along the through-plane direction. This in-plane current density profile is directly comparable with the measured one

at the GDL/CL interface due to thin membrane and CL that result in negligible electrical current along the in-plane direction.

## Results and Discussion

**Experimental validation.**— Experimental validation for the in-plane current density distribution is summarized in Fig. 2 and 3 for air and pure O<sub>2</sub>, respectively. In the case of the air cathode, reasonable agreement is achieved for all current densities, in terms of both the magnitude and shape. At the low current density of 0.05 A/cm<sup>2</sup>, excellent agreement is achieved, and both experiment and simulation indicate a uniform distribution. At 0.2 A/cm<sup>2</sup>, the simulation and experiment agree well except in the region deep inside the inner rib. The prediction shows a reduced local current density due to limited oxygen transport there, consistent with the theoretical and experimental trends in the similar location over the outer rib. In contrast, the measured current density for locations deep inside the inner rib contradicts that over the outer rib, possibly indicative of experimental error.

At 0.4 A/cm<sup>2</sup>, both the simulation and experiment display a camel-back-shaped current distribution, with two peaks appearing near the interfaces between channel and land. The current density peak results from the intricate balance between the protonic resistance and mass transport loss. The former is high in the channel area due to the exposure to low humidity and large stoichiometry gases, whereas the latter is severe deep inside the land due to the unusually wide land used in the experimental cell. A slight difference between the simulation and experiment is that the current peak appears in the close vicinity of the channel-land interface in the simulation but locates a little inside the land in the experiment. The complex shape of the in-plane current distribution points to the probable need for spatial resolution finer than 0.5 mm and less intrusive wires for potential measurement, an experimental challenge.

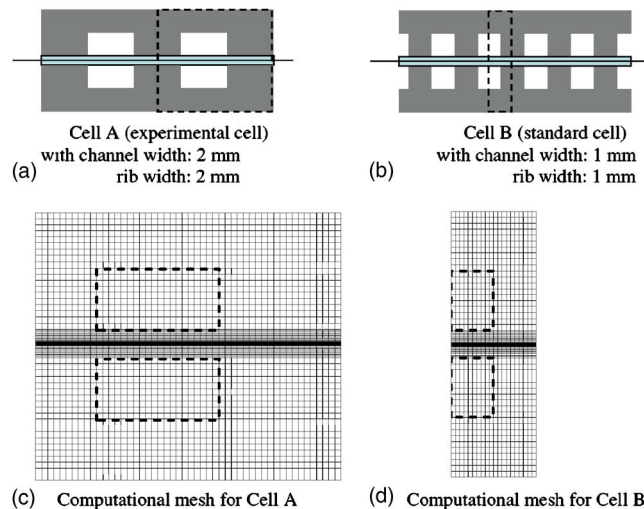


**Figure 1.** (Color online) Cross sections and computational meshes for two cell configurations.

**Table II. Cases with different cell geometries and operational conditions.**

Case no.	Cell geometry	Inlet RH	Anode	Cathode
1	Cell A	30%	H <sub>2</sub>	Air
2	Cell A	30%	H <sub>2</sub>	O <sub>2</sub>
3	Cell B	30%	H <sub>2</sub>	Air
4	Cell B	30%	H <sub>2</sub>	O <sub>2</sub>
5	Cell B	100%	H <sub>2</sub>	Air

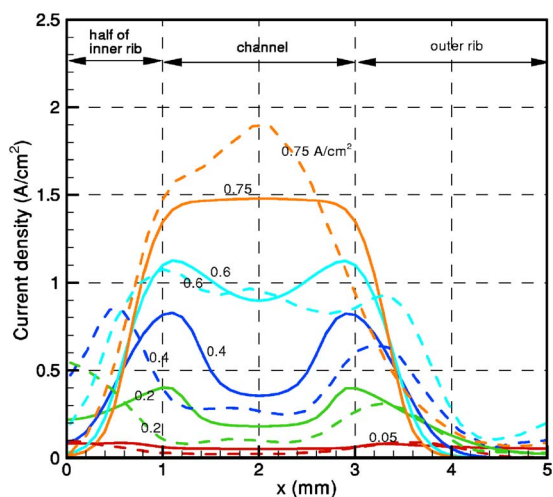


**Figure 2.** (Color online) Comparison of predicted (solid lines) and measured (dashed lines) current density profiles in the in-plane direction under air operation. Experimental data are taken from Freunberger et al.<sup>7</sup>

At 0.6 A/cm<sup>2</sup>, agreement between the predicted and measured current distributions is quite good. Moreover, the two current peaks diminish with the increasing local current density underneath the channel, due to increased water production at the higher current density which hydrates the membrane. At 0.75 A/cm<sup>2</sup>, the camel-back-shaped transitions to a single-peak profile appear in the middle of the channel. This transition is evident in both simulation and experiment, with local current density flatter in the channel area in the simulation than the experiment.

Under pure O<sub>2</sub> operation, the overall agreement is again reasonable, as shown in Fig. 3. One consistent discrepancy appears in the region deep inside the inner rib. The predicted current density there decreases towards the inside of the inner rib, evidently because the membrane is fully hydrated and the current density is controlled solely by the mass transport resistance, which becomes more severe towards the inside of the inner rib. The same trend is predicted over the outer rib. On the other hand, the experimental trends of current

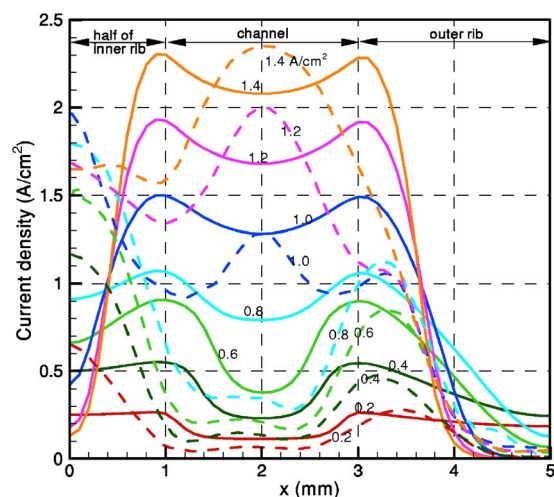


**Figure 3.** (Color online) Comparison of predicted (solid lines) and measured (dashed lines) current density profiles in the in-plane direction under O<sub>2</sub> operation. Experimental data are taken from Freunberger et al.<sup>7</sup>

distribution over the inner rib differ from the outer rib. This inconsistency in the experimental data may be indicative of gross uncertainty in the measurements and the inverse method of determining the current distribution. Another possible explanation may be the fact that GDL compression over the outer rib is greater than that over the inner rib. Therefore, better agreement in the current density over the inner rib could be expected if the GDL compression over the inner rib was adjusted appropriately in the numerical simulation.

Another discrepancy between the measured and predicted current distributions is observed in the center of the channel. A current peak appears in the experiments when the average current density exceeds 1 A/cm<sup>2</sup>. But this current peak does not appear in the simulations until 1.4 A/cm<sup>2</sup>, although the current density profile becomes increasingly flatter underneath the channel. Exact reasons for this discrepancy are unclear at present, although it was specifically pointed out by Freunberger et al.<sup>7</sup> that the current density measurements in the center of the channel were subject to more uncertainties. More theoretical and experimental research is needed to fully clarify this discrepancy.

Despite these differences, general agreement between the simulation and experiments is reasonably good for both air and O<sub>2</sub> operation. Figure 3 further indicates great nonuniformity in local current density that varies from zero over some portion of the ribs to 2.3 A/cm<sup>2</sup>. Existence of such nonuniform current distribution in the in-plane direction underscores the importance of computer-aided engineering and optimization for performance and durability improvements.

The *I-V* curves predicted for the experimental cell (cell A) under both air and O<sub>2</sub> operations are displayed in Fig. 4, clearly illustrating the positive effect of pure O<sub>2</sub>. Under O<sub>2</sub> operation, the cell voltage gains 70 mV at 0.4 A/cm<sup>2</sup> and the limiting current density is also significantly extended due to low mass transport resistance.

The liquid water saturation contours for cases 1 and 2 are shown in Fig. 5 and 6, respectively, for various current densities. In both cases, the water saturation levels at the cathode GDL/CL interface under the channel increase with the current density, since more water is generated in the cathode CL. The liquid water saturation is always higher under the rib than under the channel because of less water removal under the rib. From Fig. 5c-e it is also seen that water is transported from the cathode to anode side beneath the rib under back diffusion and hydraulic permeation that dominate over the electro-osmotic drag. The water under the anode rib is then transported in the GDL towards the anode channel by capillary forces, keeping the anode side of the membrane relatively hydrated despite the exposure to the dry gas flowing in the anode channel. Comparing

**Table III. Geometrical and operational conditions.**

Description	Value
Active area	1 cm × 1 cm = 1 cm <sup>2</sup>
Channel depth	1 mm
Channel shape	Straight
Anode/cathode GDL thickness	0.2 mm
Anode/cathode CL thickness	0.01 mm
Membrane thickness	0.05 mm
Porosity of anode/cathode GDL	0.5
Porosity of anode/cathode CL	0.5
Volume fraction of ionomer in CL	0.25
Thermal conductivity of membrane	0.95 W/m K
Thermal conductivity of CL	3.0 W/m K
Thermal conductivity of GDL	3.0 W/m K
Thermal conductivity of bipolar plate	20.0 W/m K
Hydraulic permeability of anode/cathode GDL/CL	10 <sup>-12</sup> m <sup>2</sup>
Hydraulic permeability of membrane	5 × 10 <sup>-20</sup> m <sup>2</sup>
Contact angle of anode/cathode GDL/CL	120°
Flow direction	Counterflow
Temperature	65°C
Gas pressure	1.5 bar
Anode stoichiometry	H <sub>2</sub> : 19 at 1.4 A/cm <sup>2</sup>
Cathode stoichiometry	Air: 32 at 0.75 A/cm <sup>2</sup> Oxygen: 19 at 1.4 A/cm <sup>2</sup>

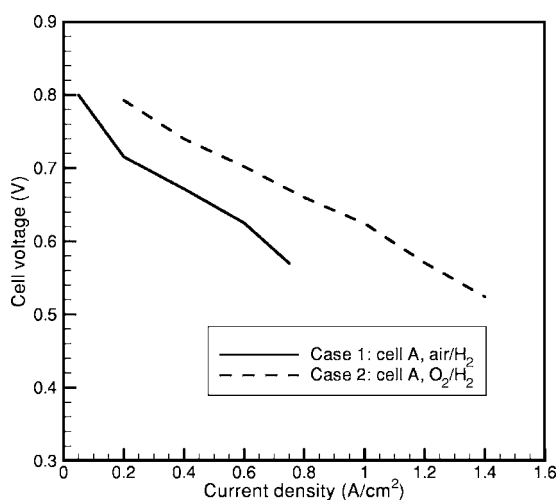


Figure 4. Predicted  $I$ - $V$  curves for air and  $O_2$  operation.

Fig. 6c with Fig. 5d, the liquid water saturation under the rib is found to be higher when operated with oxygen at the same current density of  $0.6 \text{ A/cm}^2$  as more water is generated under the rib due to larger current density there. The maximum water saturation under the rib ranges from 0.3 to 0.5 at high current densities.

The water saturation contours shown in Fig. 5 all exhibit a dry-to-wet transition from the single-phase region to the two-phase zone where liquid water coexists with the gas phase. The transition is an

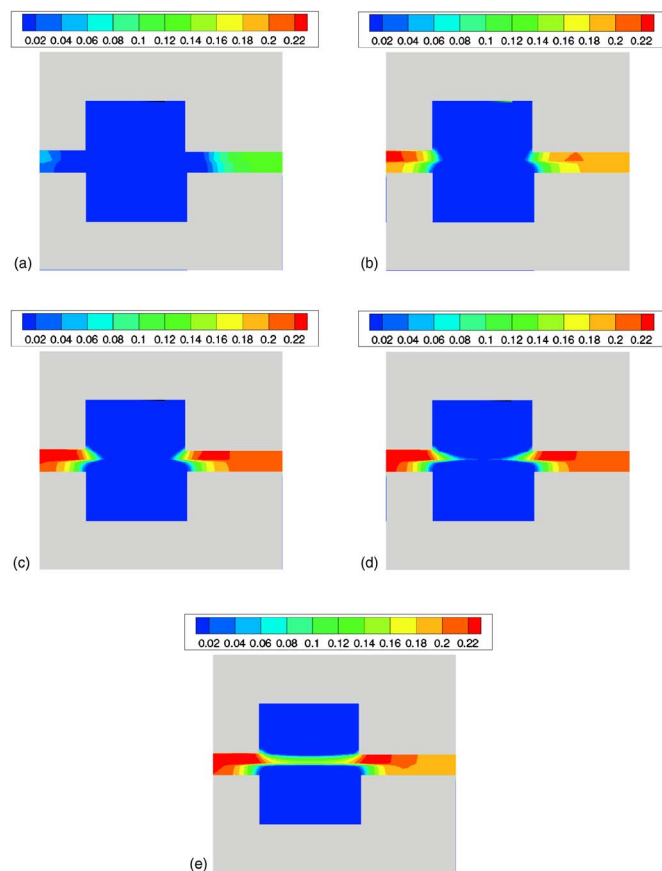


Figure 5. (Color online) Liquid water saturation distributions under air operation: (a)  $0.05 \text{ A/cm}^2$ , (b)  $0.2 \text{ A/cm}^2$ , (c)  $0.4 \text{ A/cm}^2$ , (d)  $0.6 \text{ A/cm}^2$ , and (e)  $0.75 \text{ A/cm}^2$ .

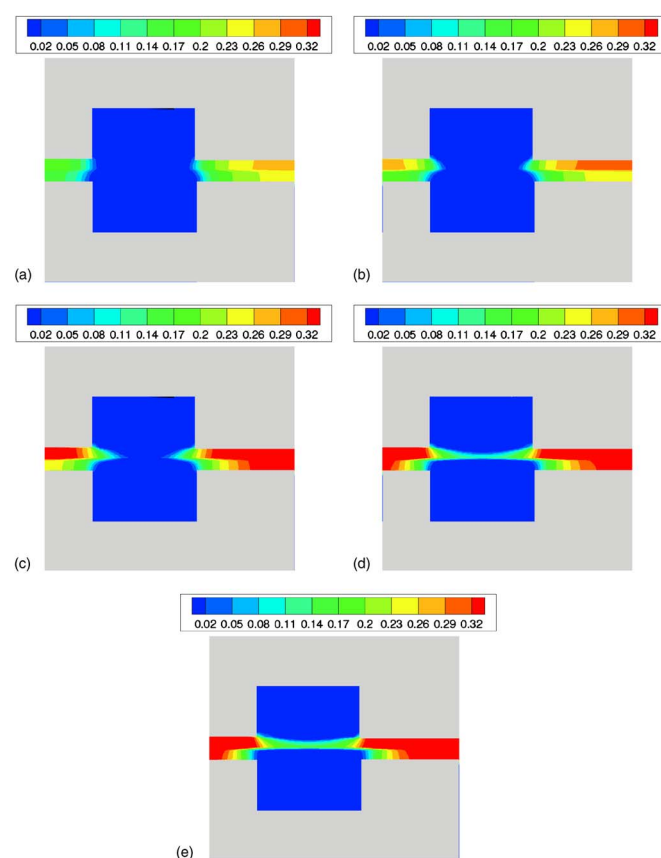
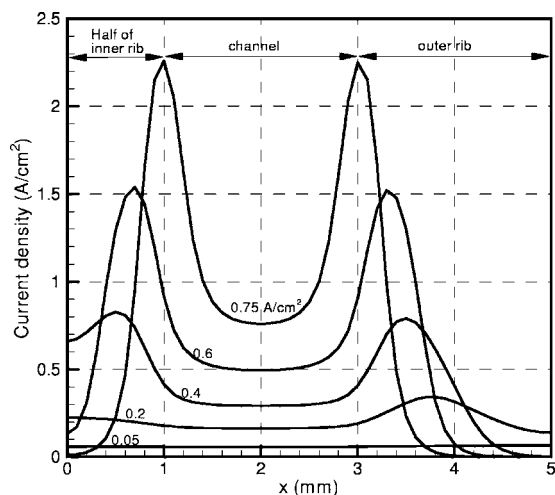


Figure 6. (Color online) Liquid water saturation distributions under  $O_2$  operation: (a)  $0.2 \text{ A/cm}^2$ , (b)  $0.4 \text{ A/cm}^2$ , (c)  $0.6 \text{ A/cm}^2$ , (d)  $1.0 \text{ A/cm}^2$ , and (e)  $1.2 \text{ A/cm}^2$ .

essential feature of the present problem as low-humidity gases flow through the channels and the wet zone arises underneath the rib areas. As a principal advantage, the present  $M^2$  model can capture the dry-to-wet transition with ease, as shown in Fig. 5.

The present model can also be used to assess the sensitivity of measurement results to possible experimental artifacts. For instance, the compression forces used in the experimental cell of Freunberger et al.<sup>7</sup> were believed to be more excessive than used in assembling standard cells due to the need to minimize the contact resistance after embedding Pt wires between the CL and GDL. For this reason a porosity of 0.5 and Bruggmann factor of 5.5 are used to mimic the high compression such that the effective water diffusivity in the GDL is given by  $D_w^{\text{eff}} = D_w(1-s)^{2.3}\epsilon^{5.5}$ . To explore the in-plane current density profile under normal compression in standard cells without intrusive instrumentation, an additional simulation has been carried out using a porosity of 0.6 and Bruggmann factor of 4. The resulting current distributions are shown in Fig. 7. In comparison to Fig. 2, it is clearly seen that the local current density at the center of the channel remains low under normal GDL compression due to high water loss to the dry gas in the channel. The camel-back shape becomes much more pronounced, even until the average current density of  $0.75 \text{ A/cm}^2$ . As discussed above, the submillimeter experimental method should be further improved by increasing the spatial resolution in order to capture the small-scale variation deep inside the rib. More accurate data of the in- and through-plane conductivity and potential may also help the measurement of current density in the middle of the channel at high load. Overall, submillimeter measurement of in-plane current distribution reveals a wealth of information on GDL and CL flooding, if properly developed and refined, it may become a quantitative, alternative approach to probing CL and GDL flooding.



**Figure 7.** In-plane current density profiles for the experimental cell under normal compression.

A comment is in order about the choice of the Bruggmann factor in the effective water diffusivity:  $D_W^{\text{eff}} = D_W(1 - s)^{2.3}e^n$ . In the absence of liquid water (i.e.,  $s = 0$ ) and with a porosity of 0.6, the Bruggmann factor between 4 and 5.5 translates to 13% and 6% of the intrinsic diffusivity, respectively. This is in good agreement with the most recent experimental finding that the ratio is roughly equal to one tenth.<sup>13</sup>

*Parametric studies.*—The experimentally validated two-phase model is used to perform parametric studies. Of particular interest is prediction and understanding of the in-plane current density profile in a standard cell with channel and rib width of 1 mm and under normal GDL compression, cell B. The performance of cell B under different operating conditions is presented in Fig. 8. It is seen that cell B under air/H<sub>2</sub> operation and 30% RH offers a larger limiting current density than cell A. The reason is that cell B has a half the rib width of cell A, thus substantially improving oxygen transport into the rib area. At the same current density, the cell voltage of cell B is also higher than cell A due to lower mass transport loss. Further reduction in channel and rib widths may result in excessive pressure drop<sup>14</sup> as well as cell voltage drop due to channel clogging by liquid water.<sup>15</sup>

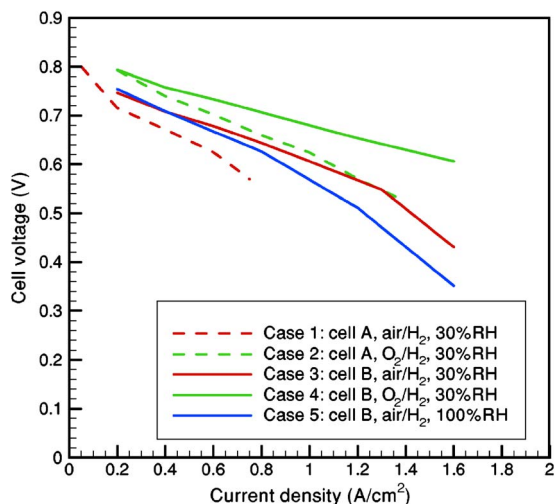


**Figure 8.** (Color online) Comparison of various  $I$ - $V$  curves.

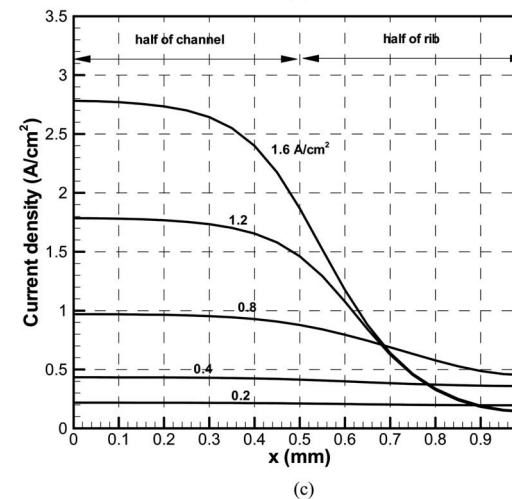
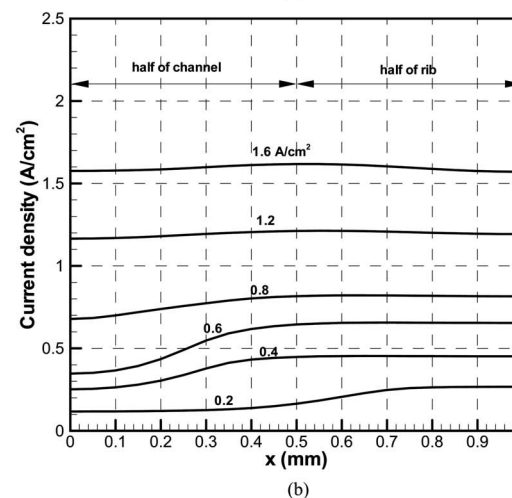
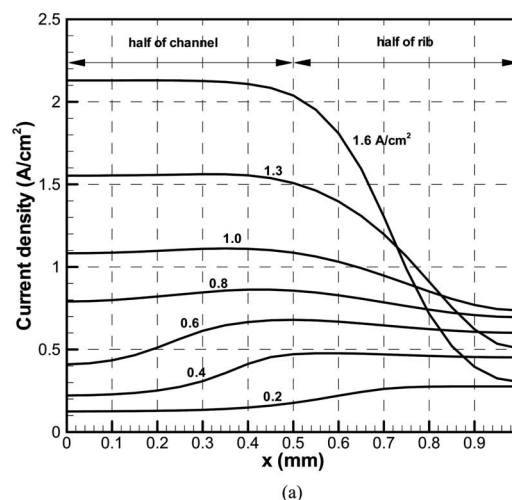


**Figure 9.** In-plane current density profiles predicted for cell B under (a) air/H<sub>2</sub> and 30% RH, (b) O<sub>2</sub>/H<sub>2</sub> and 30% RH, and (c) air/H<sub>2</sub> and 100% RH.

Figure 8 also shows that similar to the comparison of cases 1 and 2, the voltage gain for case 4 (with pure O<sub>2</sub>) is 50 mV at 0.4 A/cm<sup>2</sup> and 80 mV at 1.0 A/cm<sup>2</sup> as compared to case 3 (with air) due to higher oxygen partial pressure as well as less mass transport resistance in case 4. The oxygen gain due to the oxygen reduction reaction kinetics with a typical Tafel slope of 66 mV/dec amounts to ~45 mV. The additional gain originates from the mass transport

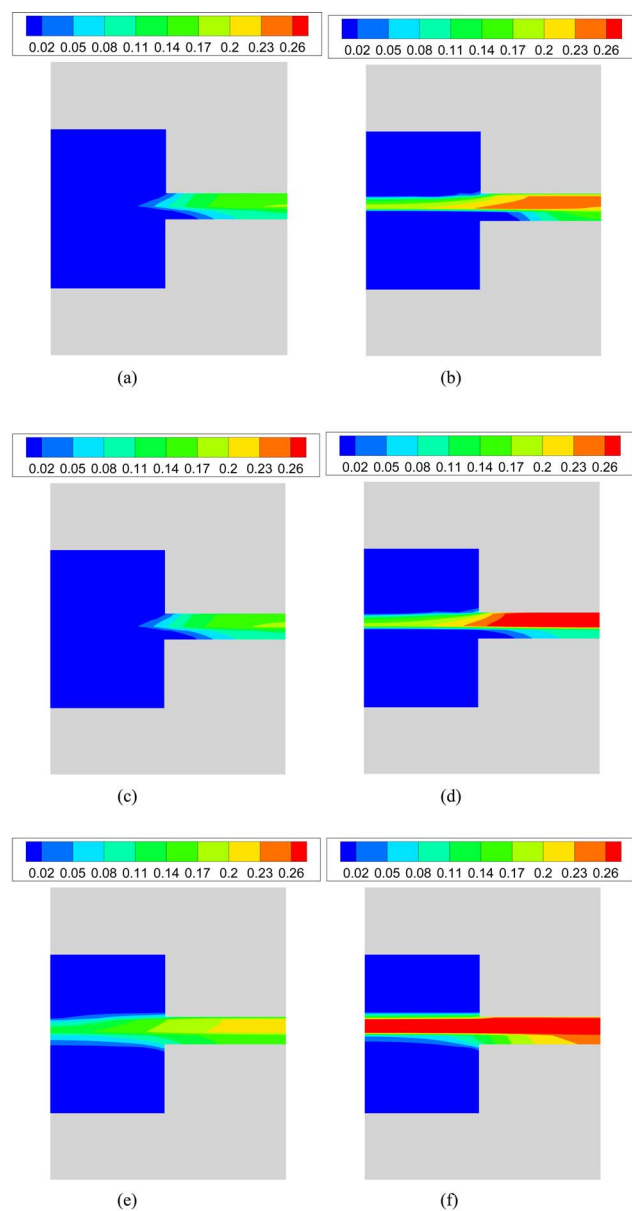


**Figure 10.** (Color online) Liquid water saturation distributions predicted for cell B under: (a) air/H<sub>2</sub>, 30% RH and  $I = 0.4 \text{ A/cm}^2$ ; (b) air/H<sub>2</sub>, 30% RH and  $I = 1.6 \text{ A/cm}^2$ ; (c) O<sub>2</sub>/H<sub>2</sub>, 30% RH and  $I = 0.4 \text{ A/cm}^2$ ; (d) O<sub>2</sub>/H<sub>2</sub>, 30% RH and  $I = 1.6 \text{ A/cm}^2$ ; (e) air/H<sub>2</sub>, 100% RH and  $I = 0.4 \text{ A/cm}^2$ ; and (f) air/H<sub>2</sub>, 100% RH, and  $I = 1.6 \text{ A/cm}^2$ .

loss. The gain in cell voltage becomes larger at higher current density, in agreement with the experimental study of Büchi et al.<sup>16</sup> which indicates that the mass transport limitation has greater impact on cell performance at higher current density. With 100% RH at the anode and cathode inlets, the cell performance surpasses the 30% RH at low current density due to better humidification of the membrane. However, as the current density exceeds  $0.4 \text{ A/cm}^2$ , the cell with fully humidified condition then exhibits a worse performance because of the severe flooding effect as predicted in Fig. 10f [cf. Fig. 10b].

The in-plane current density profiles for cases 3–5 are shown in Fig. 9. When operated with air and 30% RH, the current density peak shifts from the rib area at low current density to the channel region at high current density, reflecting the shift from ohmic control

to mass transport control. With pure oxygen and 30% inlet RH, the current density distribution has the same trend at the low current density due to the ohmic control. However, the current density remains quite flat at  $1.6 \text{ A/cm}^2$ , suggesting that the limiting current density is yet to be reached. For case 5 with air and 100% inlet RH, the oxygen diffusion is the only limitation so that the current density peak is always located under the channel. The only exception is the profile at  $0.2 \text{ A/cm}^2$ , which is quite flat since the mass transport has no effect at such a low current density.

Figure 10 presents the predicted liquid water saturation contours for cases 3–5 at current densities of  $0.4$  and  $1.6 \text{ A/cm}^2$ . It is clear that the liquid water saturation level at  $1.6 \text{ A/cm}^2$  is higher than that at  $0.4 \text{ A/cm}^2$  due to more water production [cf. Fig. 10a–f]. When operated on pure oxygen, the liquid water saturation level under the rib at  $1.6 \text{ A/cm}^2$  is higher than that with air [cf. Fig. 10b with Fig. 10d], because the current density under the rib in the former is higher. With fully humidified inlets, the predicted liquid water saturation reaches the highest levels among cases 3–5.

Overall, the in-plane current density profiles for cell B (standard cells) are significantly different from those in cell A (the experimental cell of Freunberger et al.<sup>7</sup>). This clearly indicates the strong impact of the channel/rib width on the in-plane current distribution.

## Conclusion

A validation study has been carried out to compare measured and predicted in-plane current density profiles in a differential cell configuration. Good agreement is generally found, demonstrating the validity of the M<sup>2</sup> model in the prediction of in-plane current density distribution with submillimeter resolution. Detailed liquid water saturation distributions as predicted by the model reveal that the membrane ohmic control underneath the channel interacts with the mass transport control underneath the rib, resulting in various complex shapes of the in-plane current distribution. These highly non-uniform and complex profiles call for measurement techniques with very fine spatial resolution, e.g.,  $\sim 100 \mu\text{m}$ . The in-plane current distribution reveals a wealth of information on GDL and CL flooding. Parametric studies further indicate that both GDL compression and channel/rib width play central roles in the in-plane current distribution. Therefore, these two key parameters should be carefully matched in experimental setups for current sensing.

## Acknowledgments

This work was supported by the partnership between Yuan Ze Fuel Cell Center and ECEC. Yuan Ze Fuel Cell Center acknowledges additional support by the Ministry of Education, Taiwan.

*The Pennsylvania State University assisted in meeting the publication costs of this article.*

## References

1. C. Y. Wang, *Chem. Rev. (Washington, D.C.)*, **104**, 4727 (2004).
2. H. Ju and C. Y. Wang, *J. Electrochem. Soc.*, **151**, A1954 (2004).
3. T. Araki, H. Koori, T. Taniuchi, and K. Onda, *J. Power Sources*, **152**, 60 (2005).
4. S. A. Freunberger, M. Santis, I. A. Schneider, A. Wokaun, and F. N. Büchi, *J. Electrochem. Soc.*, **153**, A396 (2006).
5. H. Ju, G. Luo, and C. Y. Wang, *J. Electrochem. Soc.*, **154**, B218 (2007).
6. K. Teranishi, S. Tsushima, and S. Hirai, *J. Electrochem. Soc.*, **153**, A664 (2006).
7. S. A. Freunberger, M. Reum, J. Evertz, A. Wokaun, and F. N. Büchi, *J. Electrochem. Soc.*, **153**, A2158 (2006).
8. H. Meng and C. Y. Wang, *J. Electrochem. Soc.*, **152**, A1733 (2005).
9. Y. Wang and C. Y. Wang, *J. Electrochem. Soc.*, **153**, A1193 (2006).
10. G. Luo, H. Ju, and C. Y. Wang, *J. Electrochem. Soc.*, **154**, B316 (2007).
11. X. G. Yang, N. A. Burke, C. Y. Wang, K. Tajiri, and K. Shinohara, *J. Electrochem. Soc.*, **152**, A759 (2005).
12. F. Q. Liu, G. Q. Lu, and C. Y. Wang, *J. Membr. Sci.*, **287**, 126 (2007).
13. X. H. Ye and C. Y. Wang, *J. Electrochem. Soc.*, **154**, B683 (2007).
14. J. Li and C. Y. Wang, Unpublished.
15. X. G. Yang, F. Y. Zhang, A. L. Lubawy, and C. Y. Wang, *Electrochem. Solid-State Lett.*, **7**, A408 (2004).
16. F. N. Büchi, S. A. Freunberger, M. Reum, G. Paganelli, A. Tsukada, P. Dietrich, and A. Delfino, *Fuel Cells*, **7**, 159 (2007).